Synthetic procedure for compound 1

Method 1

$NiCl_2 \cdot 6H_2O$ (475 mg, 2 mmol), HL^1 (252 mg, 2 mmol) and MeONa (108 mL, 2 mmol) were dissolved in MeOH (10 mL) and refluxed at 65°C for 40 minutes. After filtration and cooling to room temperature, the mother liquor was allowed to slowly diffuse with acetone vapours, affording metallic light blue crystals suitable for X-ray diffraction. Elemental analysis (%) calculated for $Ni_{14}O_{37}N_{32}C_{102}H_{176}Cl_{14}$: C, 32.57 %; H, 4.72 %; N, 11.92 %. Found: C, 32.98 %; H, 5.15 %; N, 12.02 %. Yield $\leq$ 20 %.

Method 2

$NiCl_2 \cdot 6H_2O$ (475 mg, 2 mmol), HL^2 (192 mg, 2 mmol) and NEt_3 (140 µL, 2 mmol) were dissolved in a mixture of MeOH and HCOOH (9:1 ratio, 10 mL) and stirred for 1 hour. After filtration, the mother liquor was allowed to slowly diffuse with acetone, affording metallic light blue crystals suitable for X-ray diffraction. The diffusion can also be successfully performed with Et_2O. Yield ≤ 40 %.

Method 3

$NiCl_2 \cdot 6H_2O$ (475 mg, 2 mmol) and HL^2 (192 mg, 2 mmol) were dissolved in a mixture of MeOH and HCOOH (9:1 ratio, 10 mL) and stirred for 1 hour. After filtration, the mother liquor was allowed to slowly diffuse with acetone, affording metallic light blue crystals suitable for X-ray diffraction. The diffusion can also be successfully performed with Et_2O. Yield ≤ 35 %.

Method 4

$NiCl_2 \cdot 6H_2O$ (475 mg, 2 mmol), HL^2 (192 mg, 2 mmol) and HCOONa (136 mg, 2 mmol) were dissolved in MeOH (15 mL) and stirred for 1 hour. After filtration, the mother liquor was allowed to slowly diffuse with acetone, affording metallic light blue crystals suitable for X-ray diffraction. The diffusion can also be successfully performed with Et_2O. Yield ≤ 40 %.

X-ray crystallography

A suitable crystal of **1** with dimensions 0.85 × 0.12 × 0.09 mm^3 was selected and mounted on a Rigaku Oxford Diffraction SuperNova diffractometer. The crystal was kept at a steady T = 120.15 K during data collection. The structure was solved with the ShelXT solution program using iterative methods and by using Olex2 as the graphical interface. The model was refined with ShelXL using full matrix least squares minimisation on F^2. Full details are provided in Table S1.[1-3] Powder XRD measurements were collected on freshly prepared samples of **1** using a Bruker D2 PHASER with nickel filtered Cu radiation at power 30 kW and current 10 mA. Diffraction patterns were measured from 2θ = 5° - 30°, step size 0.0101°.

Magnetic Measurements

Variable-temperature, solid-state direct current (dc) magnetic susceptibility data down to T = 1.8 K and in fields up to B = 9 T were collected on a Quantum Design PPMS Dynacool. The crystalline sample was embedded in eicosane in a gelatine capsule. Diamagnetic corrections were applied to the observed paramagnetic susceptibility.

Computational Details

Density Functional Theory (DFT) has been used to compute the magnetic exchange coupling constants on three model complexes (models **1A-C**, Figure S3) created from **1** in the Gaussian 09 suite[4] of programs. We have employed the hybrid B3LYP functional[5] together with the TZVP basis set for the Ni, Zn, Cl, O and N atoms and the SVP basis set for the C and H atoms.[6] Model **1A** is a tetra-metallic model in which the two terminal Ni^{II} ions have been replaced with two Zn^{II} ions. The latter is employed to replicate the electronic environment at the Ni^{II} centres. Models **1B-C** are pentametallic containing three Ni^{II} ions and two terminal Zn^{II} ions. To estimate the magnetic exchange coupling constants we have used Noodleman's broken symmetry approach.[7] Spin configurations used to estimate the magnetic exchange coupling constants for models **1A-C** are summarized in Table S2-3. To qualitatively explain the sign and magnitude of the magnetic interactions present we have performed overlap integral calculations using singly occupied molecular orbitals (SOMOs) of both paramagnetic centres in bimetallic models. In bimetallic complexes with bridging ligands, to split the molecule into two independent, chemically meaningful monomers, we have used broken-symmetry orbitals. As reported by Ruiz et al.,[8] the larger the overlap integral between the two orbitals the larger the J_{AF} part of the total magnetic exchange ($J = J_{AF} + J_F$). A small overlap integral means the orbitals are orthogonal and will thus add to the J_F part of the total magnetic exchange interaction.

We have employed ORCA software (version ORCA 4.0) to estimate the zero-field splitting parameters for each Ni^{II} centre. This is based on a trimetallic Zn-Ni-Zn model created from **1**.[9] The zeroth-order regular approximation (ZORA) method, together with the ZORA contracted version of the basis set (ZORA-def2-TZVPP for Ni, Zn and ZORA-def-TZVP for rest of the atoms) has been used for the resolution of identity (RI) approximation.[10] For each Ni^{II} centre during state-average complete active space self-consistent field (SA-CASSCF) calculations, we have considered eight electrons in five d-orbitals (CAS (8 electrons/5 3d-orbitals)) in the active space. Ten triplet and fifteen singlet roots are considered during CASSCF calculations. To estimate the zero-field splitting parameter accurately and consider the dynamic correlation we have performed 2^{nd} order N-electron valence perturbation theory.[11] We have used integration Grid 6 for Cl, Ni and Zn, and Grid 5 for the remaining atoms.

Table 1. Crystallographic details for compound **1**.

Compound	**1**
Formula	$C_{87}H_{140}Cl_{14}N_{24}Ni_{14}O_{34}$
$D_{calc.}$/ g cm^{-3}	1.359
μ/mm^{-1}	1.841
Formula Weight	3384.46
Colour	metallic light blue
Shape	rect. prism-shaped
Size/mm^3	0.85×0.12×0.09
T/K	120.15
Crystal System	tetragonal
Space Group	$P4_2/n$
a/Å	37.1760(2)
b/Å	37.1760(2)
c/Å	11.96640(10)
α/°	90
β/°	90
γ/°	90
V/Å^3	16538.2(2)
Z	4
Z'	0.5
Wavelength/Å	0.71073
Radiation type	Mo K_α
Θ_{min}/°	3.195
Θ_{max}/°	26.732
Measured Refl's.	152030
Indep't Refl's	17519
Refl's I≥2 σ(I)	15915
R_{int}	0.0499
Parameters	820
Restraints	25
Largest Peak	1.234
Deepest Hole	-0.615
GooF	1.172
wR_2 (all data)	0.1300
wR_2	0.1273
R_1 (all data)	0.0634
R_1	0.0570
CCDC	2169986

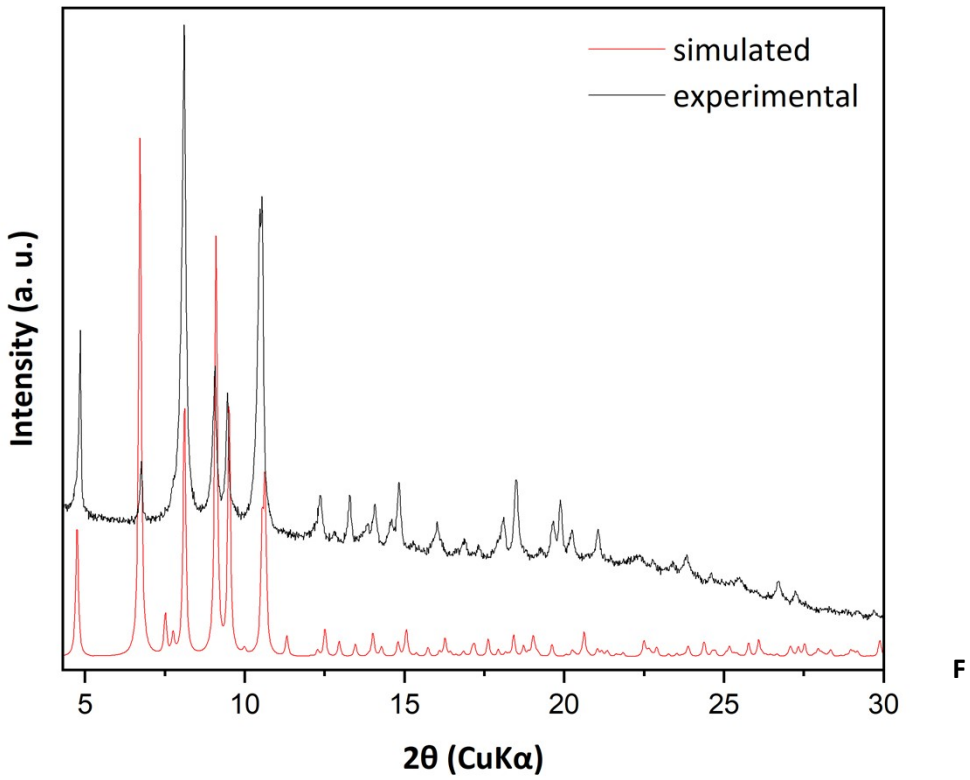

Fig. S1. Powder X-ray diffraction of **1**. Experimental data (red) and calculated (black) data.

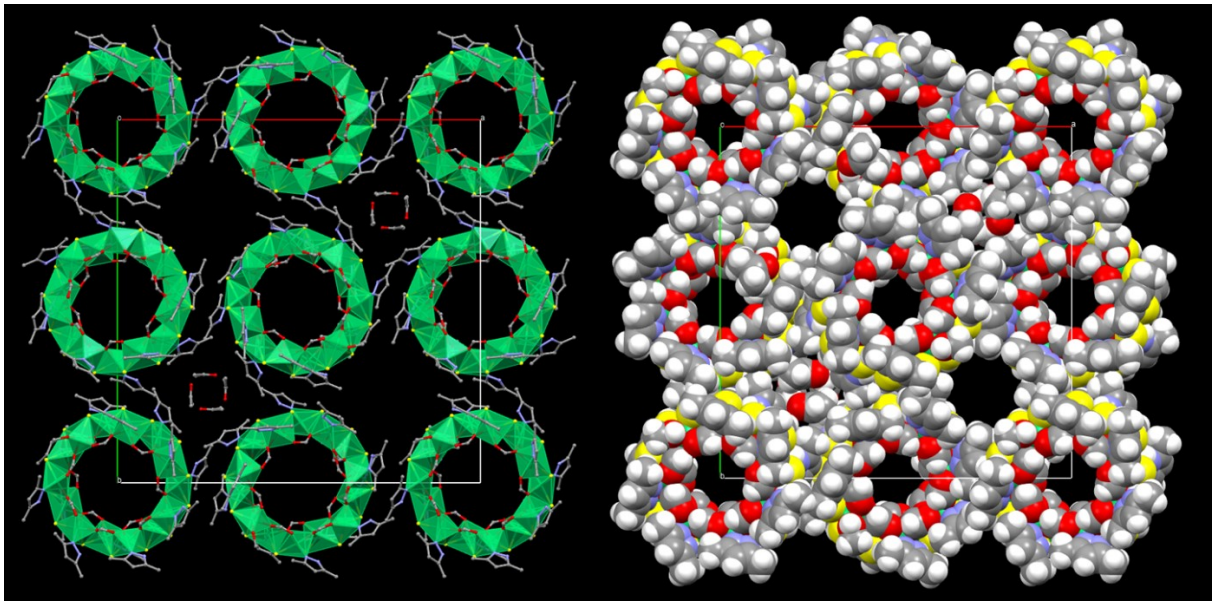

Fig. S2. The extended structure of **1** viewed down the *c*-axis of the cell in (left) polyhedral, and (right) space-filling representation. Colour code: Ni = green, O = red, N = blue, C = black, H = white, Cl = yellow.

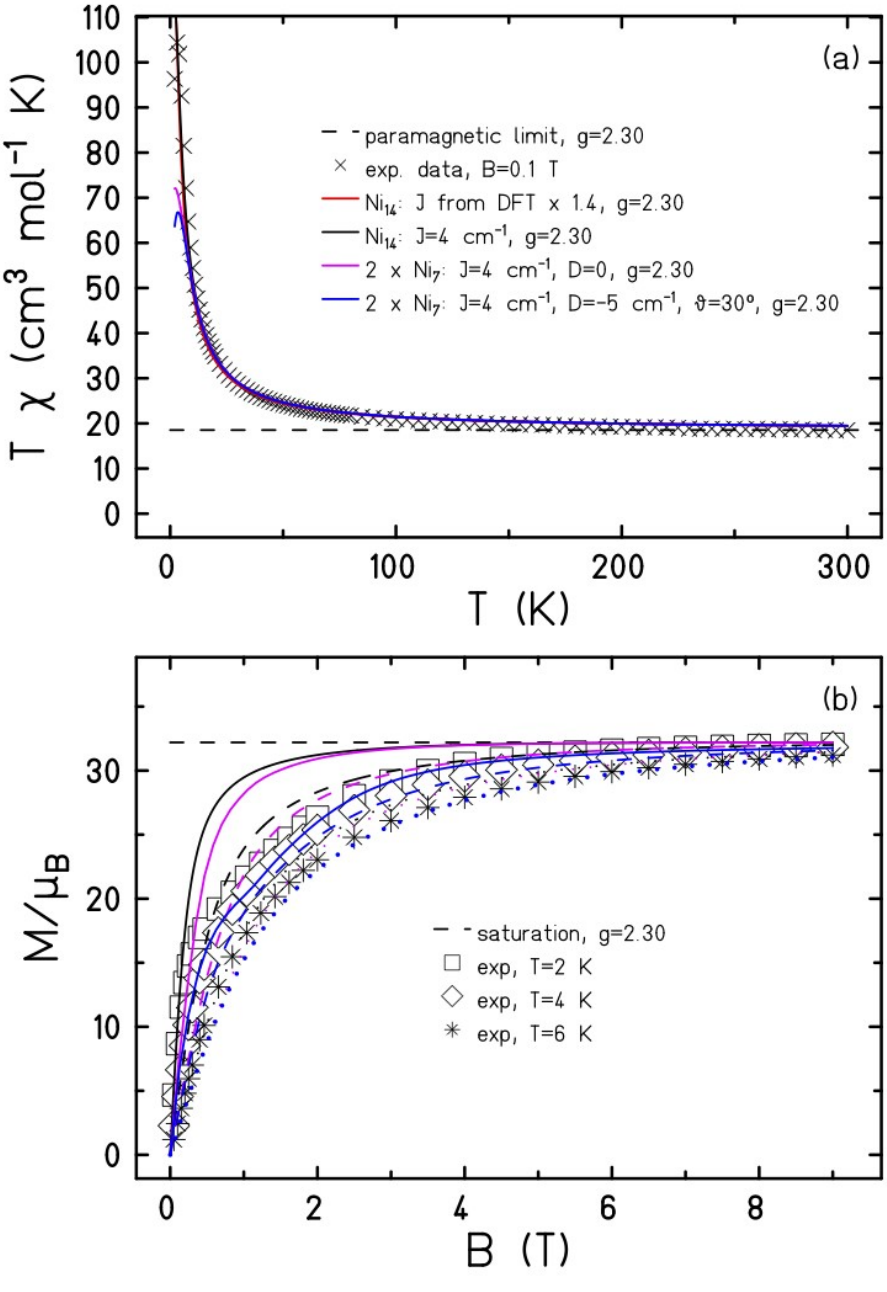

Fig. S3. Complete set of simulation data: (a) Magnetic susceptibility data potted as the χT product versus T measured in a field, B = 0.1 T between T = 300-2.0 K; red – Heisenberg Hamiltonian only with DFT exchange interactions scaled by 1.4, black – Heisenberg Hamiltonian only with the same nearest-neighbour exchange for all interactions, magenta – substitute system of 2 Ni_7 rings with only Heisenberg Hamiltonian to show that the approximation is reasonable also for the susceptibility, blue – same as magenta, but no with single-ion anisotropy. (b) M vs B data in fields B = 0.5 – 9 T and temperature range T = 1.8 - 10 K. The curves are simulations of the experimental data (solid, dashed, dotted in (b) for the three temperatures); colour code as in (a). Black and magenta are shown to demonstrate that the replacement of Ni_{14} by two Ni_7 is appropriate for the purpose. The blue curve is the major result; it proves that single-ion anisotropy has a major impact on the magnetization.

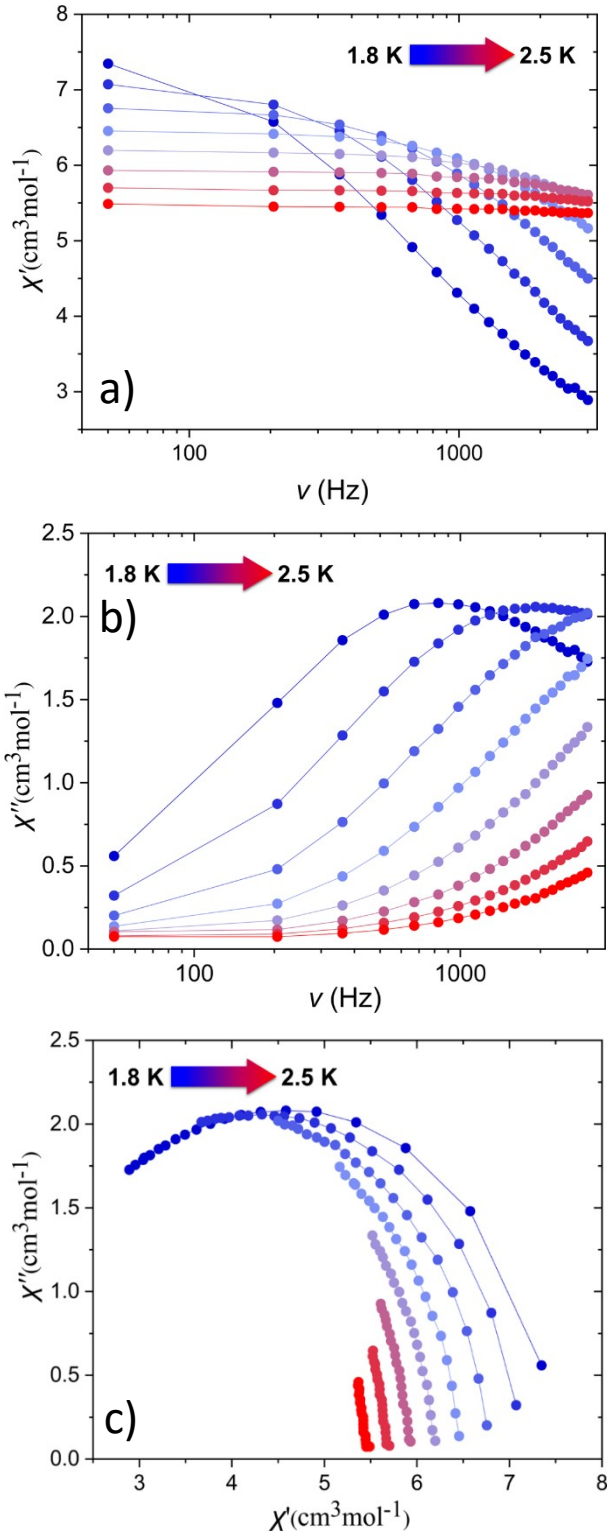

Fig.S4. (a-b) Temperature dependence of the in-phase (χ') and out-of-phase (χ'') ac susceptibility data for **1** under zero external dc field. (c) χ'' vs χ' plot of the ac magnetic susceptibility of **1** in zero dc field. The solid lines are guides.

Table S2. Spin configurations used for model **1A**. Red arrows represent spin-up and blue arrows spin-down.

	***S* value**	**Ni1**	**Ni2**	**Ni3**	**Ni4**
HS	**4**	↑	↑	↑	↑
BS-1	**2**	↓	↑	↑	↑
BS-2	**2**	↑	↓	↑	↑
BS-3	**2**	↑	↑	↓	↑
BS-4	**2**	↑	↑	↑	↓
BS-5	**0**	↓	↓	↑	↑
BS-6	**0**	↑	↓	↑	↓

Table S3. Spin configurations used for models **1B-C**. Red arrows represent spin-up and blue arrows spin-down.

	***S* value**	**Ni1**	**Ni2**	**Ni3**
HS	**3**	↑	↑	↑
BS-1	**1**	↓	↑	↑
BS-2	**1**	↑	↓	↑
BS-3	**1**	↑	↑	↓

Table S4. Pertinent structural parameters for **1** alongside the seven calculated magnetic exchange interactions, *J*.

	Avg. Ni-μ_2O/Cl distance (Å)	Ni-O-Ni angle (º)	Ni-Cl-Ni angle (º)	Ni-Cl-Ni-O Dihedral (º)	Ni···Ni distance (Å)	*J* (cm^{-1})
Ni1Ni2	2.258	105.3	83.5	17.9	3.272	+1.7
Ni2Ni3	2.249	103.5	83.2	22.3	3.237	+3.5
Ni3Ni4	2.246	102.9	83.4	17.7	3.229	+2.7
Ni4Ni5	2.250	103.1	82.6	22.5	3.228	+3.0
Ni5Ni6	2.237	103.2	83.8	19.3	3.226	+2.5
Ni6Ni7	2.233	102.5	85.1	21.0	3.234	+3.9
Ni7Ni1’	2.252	104.5	83.8	16.9	3.261	+2.1

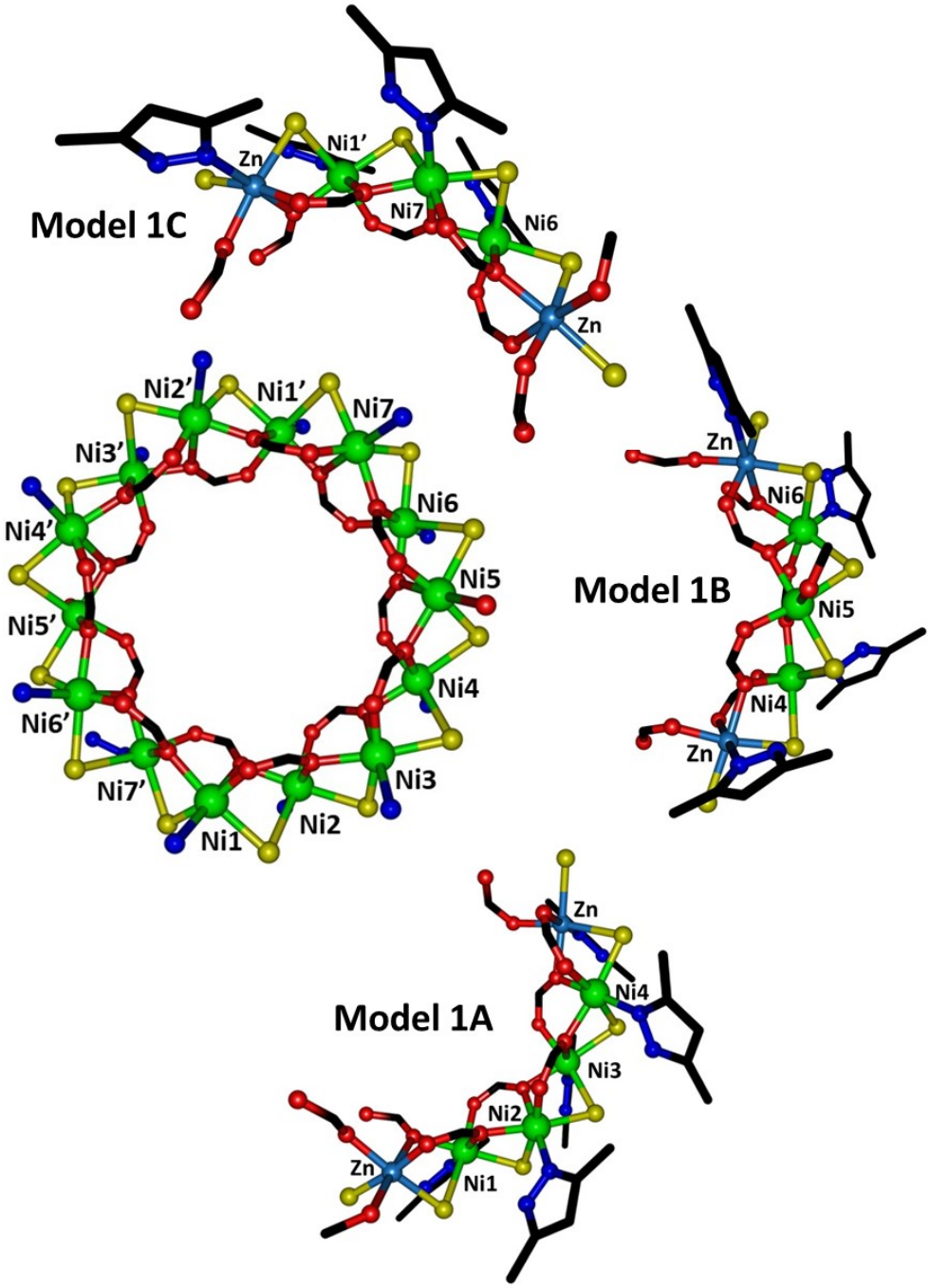

Fig. S5. Models **1A-C** on which DFT calculations have been performed in order to estimate the seven magnetic exchange interactions. Colour code: green Ni, light blue Zn, yellow Cl, red O, blue N and black C. H atoms removed for clarity.

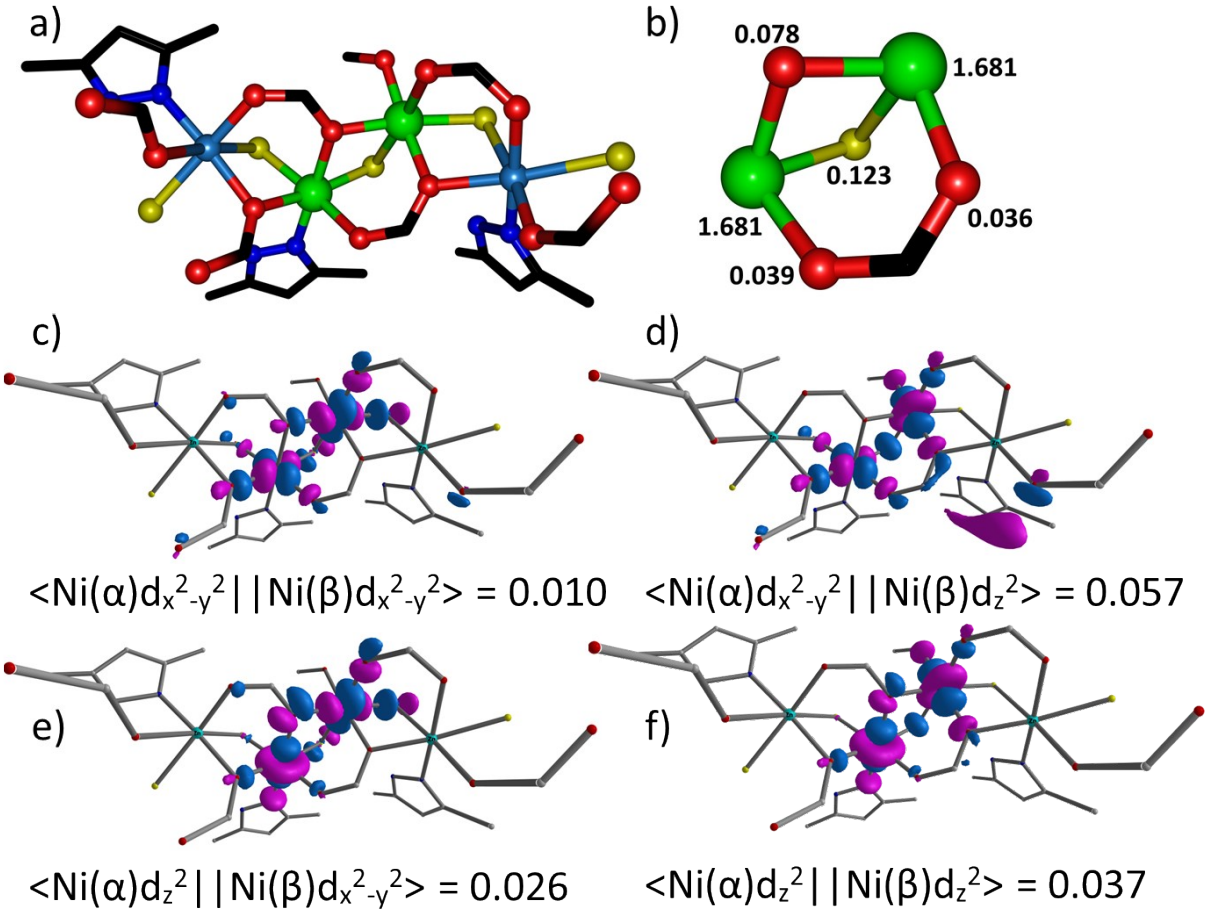

Fig. S6. (a) Model **1D** along with (b) DFT computed spin density on important atoms. Colour code is same as Figure S2. (c-f) DFT computed representative overlap integrals figures showing Ni(II) based SOMO(s)-SOMO(s) overlap interactions for **1D**. One moderate <Ni(α)$d_{x^2-y^2}$||Ni(β)d_{z^2}> and three remaining weak interactions result in weak ferromagnetic interaction.

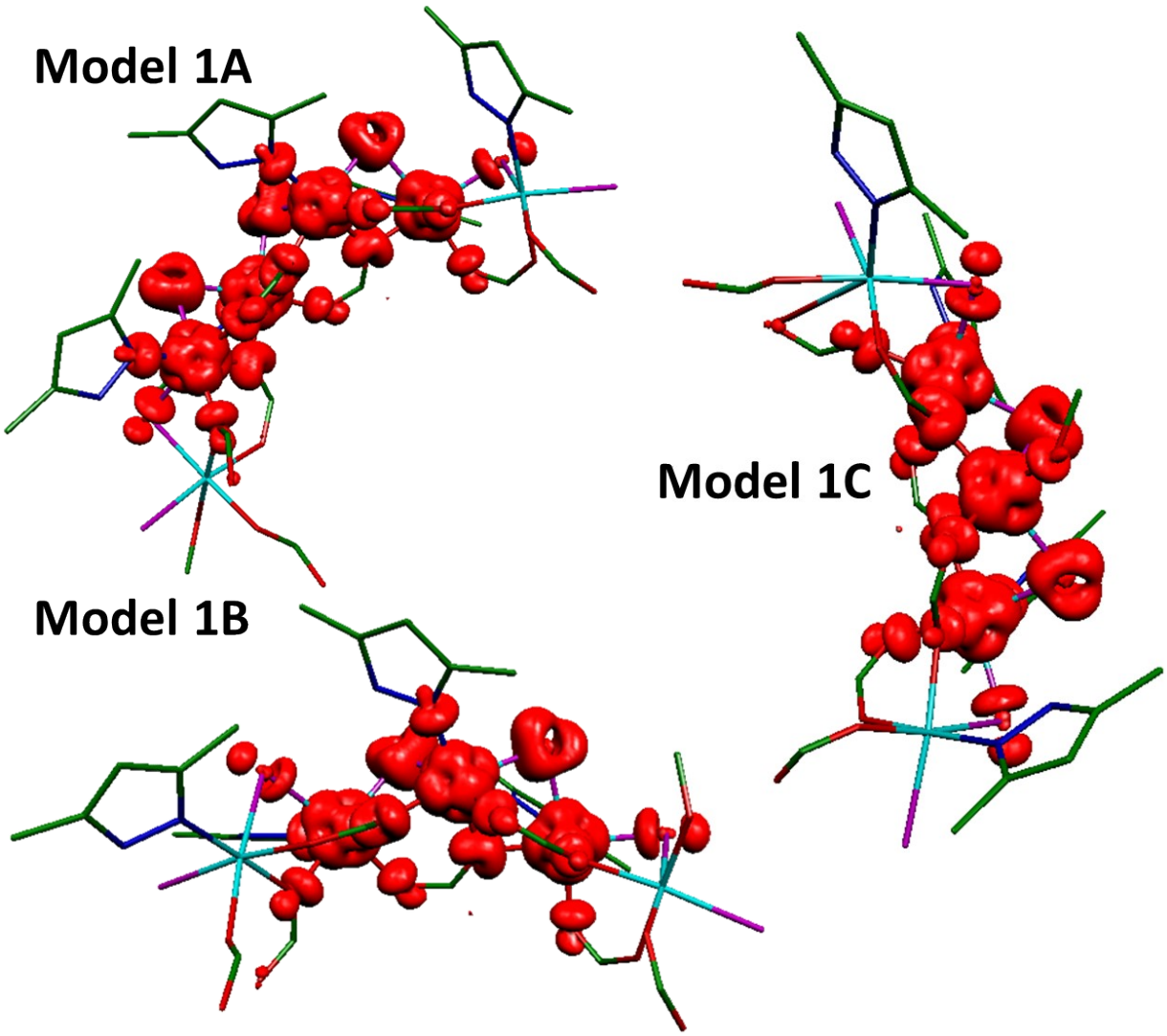

Fig. S7. DFT computed spin density plots for Models **1A-C**. The iso-density surface shown corresponds to a value of 0.003 e^{-}/bohr^3. Spin density analysis suggests strong spin delocalisation, with spin densities on the Ni^{II} ions in the range 1.668-1.682. Note that the μ-Cl ions has the largest spin density of the bridging atoms.

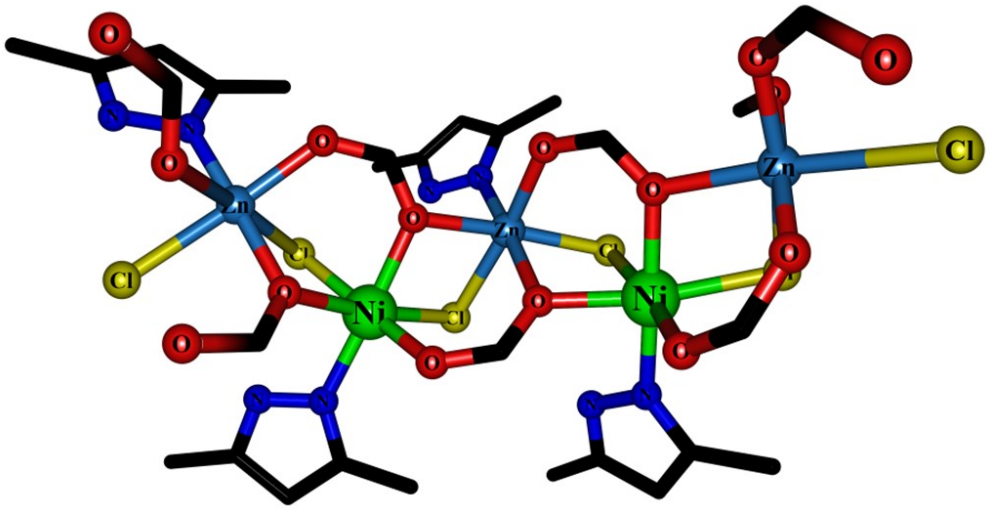

Fig. S8. Model **1E** on which we have estimated the next-nearest neighbour magnetic exchange interaction. The paramagnetic centres are connected through an syn, anti-formate group (Ni-O-C-O-Ni) resulting in a very small ferromagnetic interaction (J = +0.5 cm^{-1}).

Table S5. SHAPE analysis performed on all seven unique Ni centres in **1**.[12] The distorted octahedral environment in each case would be expected to lead to small ZFS parameters ($|D| \leq 10$ cm^{-1}).[11]

HP-6	1 D6h	Hexagon			
PPY-6	2 C5v	Pentagonal pyramid			
OC-6	3 Oh	Octahedron			
TPR-6	4 D3h	Trigonal prism			
JPPY-6	5 C5v	Johnson pentagonal pyramid J2			
Structure [ML6]	HP-6	PPY-6	OC-6	TPR-6	JPPY-6
Ni1-Ni14 ,	31.122,	27.597,	1.011,	15.290,	30.845
Ni2-Ni14 ,	30.989,	27.949,	0.969,	15.351,	31.123
Ni3-Ni14 ,	30.860,	27.995,	1.035,	15.531,	31.002
Ni4-Ni14 ,	31.301,	28.228,	0.905,	16.029,	31.248
Ni5-Ni14 ,	31.265,	27.951,	0.920,	15.237,	31.245
Ni6-Ni14 ,	30.868,	28.126,	0.950,	15.431,	31.316
Ni7-Ni14 ,	30.666,	26.969,	1.060,	15.159,	30.081

Table S6. The NEVPT2 excited states, multiplicity of the states and the transition energies of the ligand field states for Ni1. An electronic transition between the same M_L level magnetic orbitals results in a negative value of *D*, whereas it is positive between different M_L level magnetic orbitals. The relative small magnitude of *D* can be attributed to the large energy separation between the orbitals involved in the transitions. For the first four states the dominant electronic arrangements are $\{(d_{xz})^2(d_{yz})^2(d_{xy})^2(d_{x^2-y^2})^1(d_{z^2})^1\}$, $\{(d_{xz})^2(d_{yz})^2(d_{xy})^1(d_{x^2-y^2})^2(d_{z^2})^1\}$, $\{(d_{xz})^2(d_{yz})^1(d_{xy})^2(d_{x^2-y^2})^2(d_{z^2})^1\}$ and $\{(d_{xz})^1(d_{yz})^2(d_{xy})^2(d_{x^2-y^2})^2(d_{z^2})^1\}$. The major contribution to the negative *D* parameter is coming from the ground to the first excited state electronic transition ($d_{xy} \rightarrow d_{x^2-y^2}$). The electronic transitions from the ground to the second and third excited states ($d_{xz/yz} \rightarrow d_{x^2-y^2}$) contribute to positive *D* values.

D = - 4.9 cm^{-1}; E/D = 0.28 g_{xx}, g_{yy}, g_{zz} (g_{iso}) = 2.233, 2.253, 2.280 (2.255) Energies of d_{xz} (0.0), d_{yz} (168.9), d_{xy} (722.7), $d_{x^2-y^2}$ (7001.9) and d_{z^2} (8745.4) orbitals in cm^{-1}				
NEVPT2 excited states	Multiplicity	NEVPT2 energy levels cm^{-1}	Contribution to *D* cm^{-1}	Contribution to *E* cm^{-1}
0	3	0.0	0.0	0.0
1	3	8135.9	-50.9	0.1
2	3	8914.9	23.2	-23.3
3	3	9708.9	21.1	21.4
4	3	14614.9	0.3	0.1
5	3	15465.4	0.0	0.0
6	1	15674.8	0.0	0.0
7	3	15772.6	0.0	0.0
8	1	15951.6	0.0	0.0
9	1	23575.5	15.0	0.0
10	1	24237.8	-7.2	6.5
11	1	24975.2	-6.9	-6.1
12	3	26218.7	0.0	0.0
13	1	26629.7	0.0	0.0
14	3	26848.8	0.0	0.0
15	3	27293.0	0.0	0.0
16	1	29213.6	0.0	0.0
17	1	30458.6	0.0	0.0
18	1	31047.5	0.0	0.0
19	1	36123.6	0.0	0.0
20	1	36234.9	0.2	0.0
21	1	36631.5	0.1	-0.2
22	1	37073.0	0.2	0.3
23	1	37339.4	-0.7	-0.3
24	1	63581.7	0.0	0.0

Table S7. The NEVPT2 excited states, multiplicity of the states and the transition energies of the ligand field states for Ni2.

D = - 4.7 cm^{-1}; E/D = 0.22 g_{xx}, g_{yy}, g_{zz} (g_{iso})= 2.233, 2.248, 2.276 (2.252) Energies of d_{xz} (0.0), d_{yz} (268.1), d_{xy} (798.0), $d_{x^2-y^2}$ (7258.5) and d_{z^2} (8737.9) orbitals in cm^{-1}				
NEVPT2 excited states	Multiplicity	NEVPT2 energy levels cm^{-1}	Contribution to D cm^{-1}	Contribution to E cm^{-1}
0	3	0.0	0.0	0.0
1	3	8259.5	-50.3	-0.1
2	3	9180.6	22.5	-22.3
3	3	9661.3	21.4	20.9
4	3	14842.5	0.2	0.2
5	3	15479.5	0.0	0.0
6	1	15774.3	0.0	0.0
7	3	15877.0	0.0	0.0
8	1	15928.1	0.0	0.0
9	1	23714.2	15.0	0.0
10	1	24521.5	-7.1	5.0
11	1	24841.4	-7.0	-4.6
12	3	26392.7	0.0	0.0
13	1	26575.0	0.0	0.0
14	3	26944.3	0.0	0.0
15	3	27321.4	0.0	0.0
16	1	29678.3	0.0	0.0
17	1	30129.2	0.0	0.0
18	1	31043.3	0.0	0.0
19	1	36237.3	0.0	0.0
20	1	36320.4	0.4	0.0
21	1	36762.7	-0.7	-0.7
22	1	37252.5	0.9	-0.2
23	1	37486.5	-0.8	0.7
24	1	63667.0	0.0	0.0

Table S8. The NEVPT2 excited states, multiplicity of the states, along with the transition energies of the ligand field states for Ni3.

D = - 6.5 cm^{-1}; E/D = 0.19 g_{xx}, g_{yy}, g_{zz} (g_{iso})= 2.227, 2.243, 2.285 (2.252) Energies of d_{xz} (0.0), d_{yz} (344.1), d_{xy} (931.1), $d_{x^2-y^2}$ (7114.8) and d_{z^2} (9128.9) orbitals in cm^{-1}				
NEVPT2 excited states	Multiplicity	NEVPT2 energy levels cm^{-1}	Contribution to D cm^{-1}	Contribution to E cm^{-1}
Ground state	3	0.0	0.0	0.0
1	3	8014.8	-52.2	0.0
2	3	9363.8	22.5	-21.3
3	3	9799.3	20.8	19.5
4	3	14962.1	0.4	0.4
5	3	15536.6	0.0	0.0
6	1	15602.4	0.0	0.0
7	1	15911.3	0.0	0.0
8	3	16072.3	0.0	0.0
9	1	23490.2	15.3	0.0
10	1	24655.1	-7.1	4.4
11	1	24944.9	-6.9	-4.0
12	3	26323.1	0.0	0.0
13	1	26742.7	0.0	0.0
14	3	27071.2	0.0	0.0
15	3	27558.5	0.0	0.0
16	1	29591.2	0.0	0.0
17	1	30146.1	0.0	0.0
18	1	31434.4	0.0	0.0
19	1	36256.2	0.3	0.0
20	1	36434.3	0.2	0.0
21	1	36832.2	-0.9	-0.9
22	1	37423.9	0.9	-0.1
23	1	37688.1	-0.9	0.8
24	1	63762.7	0.0	0.0

Table S9. The NEVPT2 excited states, multiplicity of the states, along with the transition energies of the ligand field states for Ni4.

D = - 6.5 cm^{-1}; E/D = 0.16 g_{xx}, g_{yy}, g_{zz} (g_{iso})= 2.223, 2.238, 2.279 (2.247) Energies of d_{xz} (0.0), d_{yz} (320.1), d_{xy} (828.9), $d_{x^2-y^2}$ (7279.4) and d_{z^2} (9225.3) orbitals in cm^{-1}				
NEVPT2 excited states	Multiplicity	NEVPT2 energy levels cm^{-1}	Contribution to D cm^{-1}	Contribution to E cm^{-1}
0	3	0.0	0.0	0.0
1	3	8185.6	-50.4	-0.2
2	3	9537.3	21.2	-21.1
3	3	10038.6	20.4	19.8
4	3	15238.7	0.4	0.3
5	1	15621.5	0.0	0.0
6	3	15805.8	0.0	0.0
7	1	15919.3	0.0	0.0
8	3	16379.9	0.0	0.0
9	1	23676.8	15.2	0.0
10	1	24807.9	-7.0	4.5
11	1	25226	-6.8	-4.2
12	3	26597.9	0.0	0.0
13	1	26774.1	0.0	0.0
14	3	27281.3	0.0	0.0
15	3	27794.3	0.0	0.0
16	1	29656	-0.1	-0.1
17	1	30531.5	0.0	0.0
18	1	31439	0.0	0.0
19	1	36610.7	0.2	0.0
20	1	36818.4	0.1	0.0
21	1	37197.4	-0.4	-0.7
22	1	37714	0.4	0.3
23	1	37960.6	-0.7	0.5
24	1	63988.5	0.0	0.0

Table S10. The NEVPT2 excited states, multiplicity of the states, along with the transition energies of the ligand field states for Ni5.

D = - 1.9 cm^{-1}; E/D = 0.00 g_{xx}, g_{yy}, g_{zz} (g_{iso})= 2.250, 2.258, 2.266 (2.258) Energies of d_{xz} (0.0), d_{yz} (500.5), d_{xy} (825.4), $d_{x^2-y^2}$ (7722.2) and d_{z^2} (7972.8) orbitals in cm^{-1}				
NEVPT2 excited states	Multiplicity	NEVPT2 energy levels cm^{-1}	Contribution to D cm^{-1}	Contribution to E cm^{-1}
0	3	0.0	0.0	0.0
1	3	8620.0	-46.3	0.0
2	3	8720.8	24.3	-19.2
3	3	9114.7	24.0	19.8
4	3	14520.6	-0.1	0.0
5	3	14873.2	0.0	0.0
6	3	15413.2	0.0	0.0
7	1	15984.0	0.0	0.0
8	1	16002.3	0.0	0.0
9	1	24146.1	13.7	0.0
10	1	24162.8	-7.3	-0.7
11	1	24325.6	-6.9	0.7
12	3	26358.4	0.0	0.0
13	1	26393.8	0.0	0.0
14	3	26410.4	0.0	0.0
15	3	26911.5	0.0	0.0
16	1	29715.8	0.0	0.0
17	1	29717.9	0.0	0.0
18	1	30611.5	0.0	0.0
19	1	35603.8	0.1	0.1
20	1	36150.6	0.0	0.0
21	1	36154.0	0.3	0.0
22	1	36901.3	-0.9	0.3
23	1	36913.5	-0.9	-0.3
24	1	63435.6	0.0	0.0

Table S11. The NEVPT2 excited states, multiplicity of the states, along with the transition energies of the ligand field states for Ni6.

D = - 4.7 cm^{-1}; E/D = 0.21 g_{xx}, g_{yy}, g_{zz} (g_{iso})= 2.234, 2.247, 2.276 (2.252) Energies of d_{xz} (0.0), d_{yz} (439.3), d_{xy} (784.3), $d_{x^2-y^2}$ (7378.4) and d_{z^2} (8652.7) orbitals in cm^{-1}				
NEVPT2 excited states	Multiplicity	NEVPT2 energy levels cm^{-1}	Contribution to D cm^{-1}	Contribution to E cm^{-1}
0	3	0.0	0.0	0.0
1	3	8250.5	-50.5	0.0
2	3	9216.0	22.8	-22.3
3	3	9630.0	21.4	21.1
4	3	14844.3	0.2	0.2
5	3	15380.3	0.0	0.0
6	1	15829.7	0.0	0.0
7	3	15840.3	0.0	0.0
8	1	15947.6	0.0	0.0
9	1	23732.8	15.0	0.0
10	1	24547.0	-7.1	4.8
11	1	24795.8	-7.0	-4.5
12	3	26402.9	0.0	0.0
13	1	26527.1	0.0	0.0
14	3	26974.5	0.0	0.0
15	3	27148.7	0.0	0.0
16	1	29703.6	0.0	0.0
17	1	30301.6	0.0	0.0
18	1	30743.0	0.0	0.0
19	1	36073.8	0.3	0.0
20	1	36457.1	0.1	0.0
21	1	36662.7	-1.0	-0.9
22	1	37230.7	1.3	0.0
23	1	37354.6	-0.9	0.7
24	1	63622.3	0.0	0.0

Table S12. The NEVPT2 excited states, multiplicity of the states, along with the transition energies of the ligand field states for Ni7.

D = - 5.1 cm^{-1}; E/D = 0.29 g_{xx}, g_{yy}, g_{zz} (g_{iso})= 2.226, 2.248, 2.275 (2.249) Energies of d_{xz} (0.0), d_{yz} (344.3), d_{xy} (824.0), $d_{x^2-y^2}$ (7308.0) and d_{z^2} (9006.2) orbitals in cm^{-1}				
NEVPT2 excited states	Multiplicity	NEVPT2 energy levels cm^{-1}	Contribution to D cm^{-1}	Contribution to E cm^{-1}
0	3	0.0	0.0	0.0
1	3	8289.9	-49.3	0.2
2	3	9140.0	22.0	-22.5
3	3	10003.7	20.6	20.7
4	3	14982.3	0.2	0.1
5	1	15663.7	0.0	0.0
6	3	15665.9	0.0	0.0
7	1	15941.8	0.0	0.0
8	3	16184.0	0.0	0.0
9	1	23755.9	15.0	0.0
10	1	24437.3	-7.1	6.4
11	1	25244.3	-6.8	-6.0
12	3	26441.5	0.0	0.0
13	1	26652.7	0.0	0.0
14	3	27245.6	0.0	0.0
15	3	27476.9	0.0	0.0
16	1	29344.1	0.0	0.0
17	1	30825.0	0.0	0.0
18	1	31022.1	0.0	0.0
19	1	36365.6	0.1	0.0
20	1	36697.4	0.0	0.1
21	1	36946.7	-0.4	-0.3
22	1	37515.7	0.5	0.3
23	1	37717.5	-0.5	-0.2
24	1	63807.0	0.0	0.0

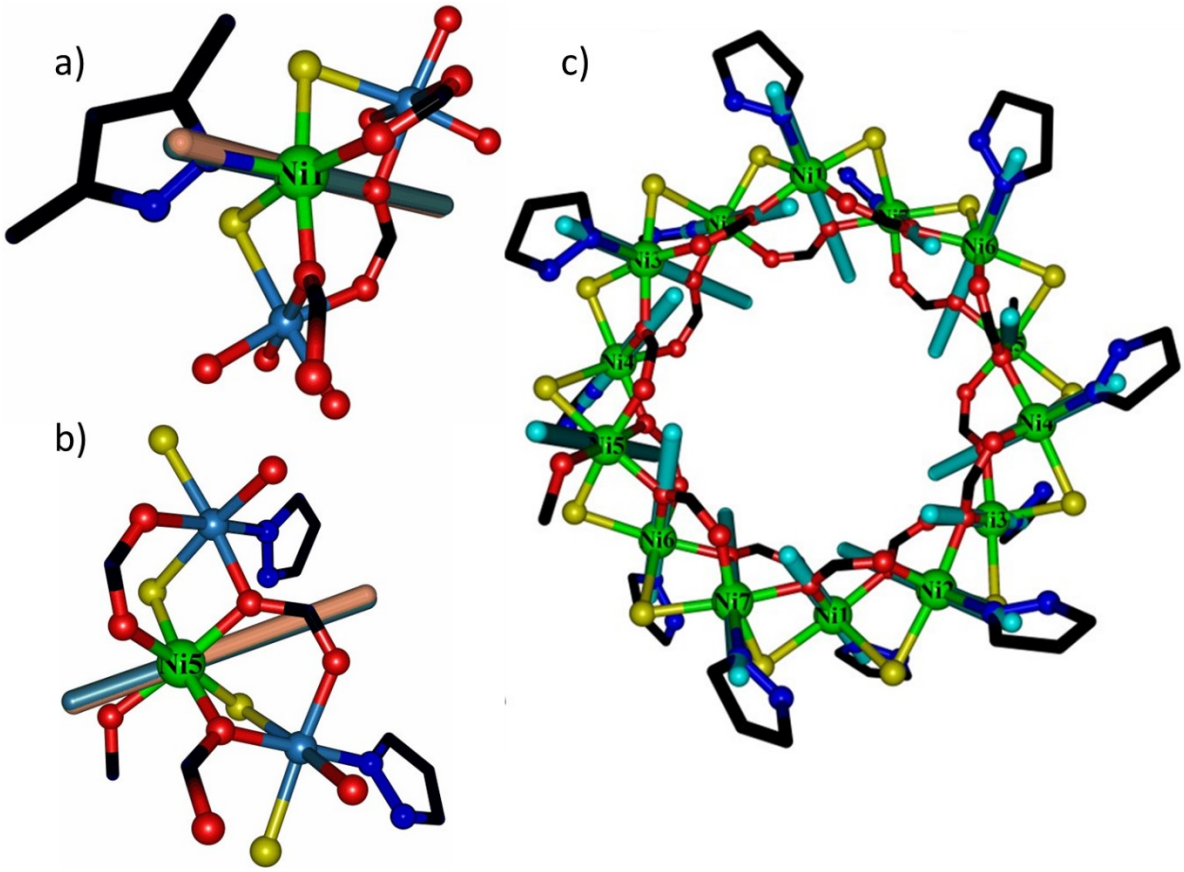

Fig. S9. The NEVPT2 computed D_{zz} (cyan coloured bars) and g_{zz} axes (brown coloured bars) for (a) Ni1, (b) Ni5 and (c) **1**. Note that all the Ni^{II} ions have both (coincident) D_{zz} and g_{zz} axes oriented along N atom of HL and an O atom of a formate, with the exception of Ni5 where both axes are slightly tilted away from the donor atoms.

References

1. G. M. Sheldrick, *Acta Cryst.*, 2015, **A71**, 3-8.

2. O. V. Dolomanov, L. J. Bourhis, R. J. Gildea, J. A. K. Howard and H. Puschmann, *J. Appl. Cryst.*, 2009, **42**, 339-341.

3. G. M. Sheldrick, *Acta Cryst.*, 2015, **C71**, 3-8.

4. M. J. Frisch, G. W. Trucks, H. B. Schlegel, G. E. Scuseria, M. A. Robb, J. R. Cheeseman, G. Scalmani, V. Barone, B. Mennucci, G. A. Petersson, H. Nakatsuji, M. Caricato, X. Li, H. P. Hratchian, A. F. Izmaylov, J. Bloino, G. Zheng, J. L. Sonnenberg, M. Hada, M. Ehara, K. Toyota, R. Fukuda, J. Hasegawa, M. Ishida, T. Nakajima, Y. Honda, O. Kitao, H. Nakai, T. Vreven, J. A. Montgomery, Jr., J. E. Peralta, F. Ogliaro, M. Bearpark, J. J. Heyd, E. Brothers, K. N. Kudin, V. N. Staroverov, T. Keith, R. Kobayashi, J. Normand, K. Raghavachari, A. Rendell, J. C. Burant, S. S. Iyengar, J. Tomasi, M. Cossi, N. Rega, J. M. Millam, M. Klene, J. E. Knox, J. B. Cross, V. Bakken, C. Adamo, J. Jaramillo, R. Gomperts, R. E. Stratmann, O. Yazyev, A. J. Austin, R. Cammi, C. Pomelli, J. W. Ochterski, R. L. Martin, K. Morokuma, V. G. Zakrzewski, G. A. Voth, P. Salvador, J. J. Dannenberg, S. Dapprich, A. D. Daniels, O. Farkas, J. B. Foresman, J. V. Ortiz, J. Cioslowski, and D. J. Fox, Gaussian, Inc., Wallingford CT, 2013.

5. (a) A. D. Becke, *Phys. Rev. A*, 1988, **38**, 3098-3101; b) A. D. Becke, *J. Chem. Phys.*, 1993, **98**, 5648; c) C. Lee, W. Yang and R. G. Parr, *Phys. Rev. B: Condens. Matter Mater. Phys.*, 1988, **37**, 785.

6. (a) A. Schäfer, H. Horn and R. Ahlrichs, *J. Chem. Phys.,* 1992, **97**, 2571; (b) A. Schafer, C. Huber and R. Ahlrichs, *J. Chem. Phys.,* 1994, **100**, 5829–5835.

7. L. Noodleman, *J. Chem. Phys.*, 1981, **74**, 5737.

8. C. Desplanches, E. Ruiz, A. Rodríguez-Fortea and S. Alvarez, *J. Am. Chem. Soc.*, 2002, **124**, 5197-5205.

9. F. Neese, *Wiley Interdiscip. Rev. Comput. Mol. Sci.,* 2012, **2**, 73–78.

10. (a) K. Eichkorn, O. Treutler, H. Öhm, M. Häser and R. Ahlrichs, *Chem. Phys. Lett.,* 1995, **242**, 652–660; (b) K. Eichkorn, F. Weigend, O. Treutler and R. Ahlrichs, *Theor. Chem. Acc.,* 1997, **97**, 119–124.

11. (a) C. Angeli, R. Cimiraglia, S. Evangelisti, T. Leininger and J.-P. Malrieu, *J. Chem. Phys.,* 2001, **114**, 10252; (b) C. Angeli, R. Cimiraglia and J.-P. Malrieu, *J. Chem. Phys.*, 2002, **117**, 9138; (c) C. Angeli, R. Cimiraglia and J.-P. Malrieu, *Chem. Phys. Lett.,* 2001, **350**, 297–305.

12. SHAPE, version 2.0; continuous shape measures calculation; Electronic Structure Group, Universiat de Barcelona: Barcelona, Spain, 2010.